Flood Sequence Mapping with Multimodal Remote Sensing Under the Influence of Dense Vegetation: Mississippi River Case Study

Zhouyayan Li [a,b*], Ibrahim Demir [a,b,c]

[a] Dept. of Civil and Environmental Engineering, University of Iowa, Iowa City, Iowa, USA
[b] IIHR Hydroscience and Engineering, University of Iowa, Iowa City, Iowa, USA
[c] Dept. of Electrical and Computer Engineering, University of Iowa, Iowa City, Iowa, USA
* Corresponding Author, Email: zhouyayan-li@uiowa.edu

Abstract

Remote sensing (RS) imagery has become more and more popular in surface water extent extraction applications with the help of increasing availability of RS data and advancements in image processing algorithms, software, and hardware. Many studies have demonstrated that RS imagery has the potential to work independently or along with other well-documented approaches in identifying flood extent. However, due to the insufficiency of images from single-sourced RS and independent references for validation, most existing studies either focused on mapping a single scene or failed to support their results with adequate non-RS validation when multi-temporal/multi-spatiotemporal images were involved. Because of that, hydrosimulations still dominate flood series mapping despite requiring huge data and computational resources. To close these gaps, this study investigated the efficacy of RS-based multi-spatiotemporal flood inundation mapping using multimodal RS imageries to take advantage of improved data availability and complementary image properties. This study also proposed a Quantile-based Filling & Refining (QFR) workflow to resolve the blocking effects of dense vegetation that occurs in study areas. We tested the workflow in four lock and dam sites on the Mississippi River, downstream to the Quad City area, by comparing the RS-based flood maps with HEC-RAS simulations. Compared to the original flood extent that only went through basic post-processing, QFR maps were noticeably more consistent with HEC-RAS maps. Results also showed that all steps in QFR contributed to performance improvements. Despite all being necessary in our case, some should be adjusted in different study regions, such as the levee step. Our findings showcased the efficacy of the multimodal RS flood mapping with QFR post-processing. Due to its simple structure, the proposed workflow has potential to be fully automated and can benefit near-real-time and real-time applications.

Keywords: multimodal remote sensing; flood mapping; quantile-based correction; geo-topo analysis

1. Introduction

Flooding is one of the most devastating natural hazards due to its frequency, widespread, and overlap with the most populated areas, influencing millions of people every year and causing billions of dollars in economic losses all over the world (Wahlstrom, 2015; NOAA, n.d.; Romali & Yusop, 2021; Alabbad and Demir, 2022). Remote Sensing (RS) imageries, especially those coming from satellites, have larger coverage and better spatial and temporal consistency than many other data resources, such as crowd-sourced data (Ali & Ogie, 2017; Li et al., 2022b) or other instrumentation efforts (Muste et al., 2017). In the research domain of flood inundation mapping, RS imagery has been widely used for cross-validating with hydrologic modeling (Kim et al., 2022; Thakur et al., 2020) and serves as an independent data source for water extent extraction (Gao et al., 2018; Sai et al., 2020; Li and Demir, 2023a). Additionally, RS imagery and its products have been widely adopted as image, map, and validation resources for other data-driven models, such as in machine learning and deep learning applications (Avand et al., 2021; Costache et al., 2019; 2020) for synthetic image generation (Gautam et al., 2022) and data augmentation (Sit et al., 2023).

To date, the most documented application of RS imagery in the flood mapping domain is single-scene mapping (a scene that is captured on a specific day somewhere), such as the work done by Billah et al. (2023), Gašparovič & Klobučar (2021), and Goffi et al. (2020). Studies that involve multi-temporal RS images, such as those done by Anusha & Bharathi, (2020), Martinis et al. (2015), and Uddin et al. (2019), seldom validated their flood maps with non-RS-based references, such as flood maps from independent hydrosimulations. We believe that validating only against results derived from another RS source is insufficient, as it just means results from two (or multiple) RS imageries are consistent but does not necessarily mean they are accurate. Letting along the discrepancy of image capture time between different sensors (such as Sentinel 2, PlanetScope, SAR, and Landsat), which is commonly ignored when multiple sensors are involved (He & Yokoya, 2018; Jiang et al., 2022; Wu et al., 2022) but will lead to great uncertainty to the conclusion when one is used as the reference to validate the other.

Due to the above reasons, hydrosimulations (e.g., hydrologic and hydrodynamic modeling) remain the most widely used approaches to study the continuous changes in flood extent over a period (Li et al., 2022a). Although being accurate and well documented in the literature, the large data as well as computing requirements (Teng et al., 2017; Demir et al., 2015) have prevented those models from working for data-scarce areas or applications with limited computational power (Hu and Demir, 2021). Due to the large computational loads, those simulations often suffer from poor timeliness and thus are not suitable for near-real-time or real-time applications (Li et al., 2018; Musser et al., 2016; Li and Demir, 2022).

The development of RS technologies and the improving availability of RS imageries, especially multimodal remote sensing, have brought new possibilities to this research domain. RS-based flood mapping requires RS images as the major input and may be accompanied with a few easy to obtain auxiliary geo-spatial datasets for result refinement, which thus allows improved processing time and highly automated procedures compared to hydrosimulations.

Multimodal imageries have two extra advantages in generating flood extent series: a) exploiting complementary properties (Dalla Mura et al., 2015; Hu et al., 2023); and b) alleviating the influence of sparse visits of single RS source and thus improving data availability (Islam et al., 2020; Rambour et al., 2020). Assuming a flood event lasting for about 10 days, SAR and Landsat 8/9 satellites may only be able to visit the scene once, Sentinel-2 and PlanetScope have an improved revisit time but do not necessarily result in improved data availability, as optical sensors are prone to cloud coverage, haze, and other meteorological and illumination factors that damage the view (Yan et al., 2015; Li and Demir, 2023b). Given that, data insufficiency is highly likely an issue when we work with a single image source whereas multimodal data will allow more images to work with. Unfortunately, we believe the efficacy of multimodal RS imagery in reconstructing a flood map series during a continuous period has not been well studied in the literature, due to the limitation of the availability of both RS imageries and reference maps for validation as discussed above.

With those in mind, this study was aimed at exploring the efficacy of a multimodal RS-based workflow in reconstructing a series of flood maps documenting a flooding process lasting for several days. In addition, we introduced Quantile-based Filling & Refining (QFR) procedure that utilizes geo-topo characteristics of flooded pixels on the original RS flood maps to correct and improve the prediction in areas blocked with dense vegetation. To make the workflow transferrable to other regions and well-compatible with open RS sources, all data (except for the streamflow measurements and the reference maps) used in this study are either openly available or have multiple public alternatives. Furthermore, the workflow was kept simple and thus is easy to automate.

For the remaining sections of this paper, we will first introduce the flood event and study area, followed by an introduction of the data used. Next, we will explain the methodology in detail followed by results and corresponding discussions. Finally, we will summarize the paper with key findings and conclusions at a high level.

2. Material and Methods

2.1. Study Region and Event

The relentless rainfall in the upstream Mississippi River basin led to the river level being above the flood stage for several months during the summer and early fall of 2019. During that period, the river experienced major flooding from late May to June 2019 (US Department of Commerce, n.d.). This study focuses on the flooding that occurred from May 30 to June 13, 2019, at locations that are downstream to Quad City (a region that consists of four cities on the Illinois-Iowa border) and upstream to the most Southeast corner of Iowa. There are four locks and dams in our study area. They are Lock and Dam 16 in Illinois City, Lock and Dam 17 in New Boston, Lock and Dam 18 in Gladstone, and Lock and Dam 19 in Keokuk, from upstream to downstream. Figure 1 depicts the location of those four locks and dams. For simplicity, we will refer to them as Pool 16, 17, 18, and 19, hereinafter.

2.2. Data and Reference Flood Maps

This study involved three types of data including multimodal RS imagery (one radar and two optical imageries), streamflow measurements, and auxiliary geo-topo datasets. For RS imagery, we used ESA Sentinel-1 C-band Ground Range Detected (GRD) SAR images, ESA Sentinel-2 A/B surface reflectance images (referred to as S2), and 3-m PlanetScope scenes (referred to PS) captured by PS2 and PS2.SD satellites. Note that we only utilized the VV band of SAR images, for previous studies have reported that the VV band is more accurate than the VH band in surface flood mapping applications (Markert et al., 2020; Tiwari et al., 2020; Twele et al., 2016). For simplicity, the term 'SAR' hereinafter will refer to the VV band of those SAR images.

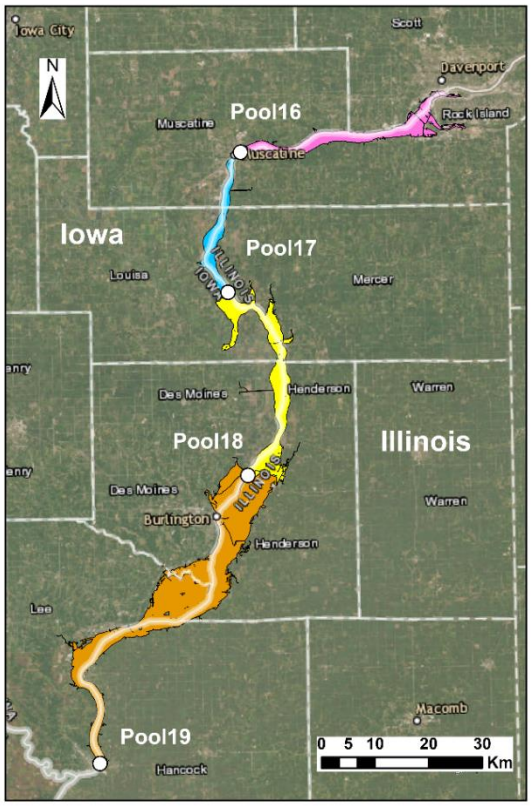

Figure 1. The study area of the Mississippi River segments, and the four Locks & Dams operated by the United States Army Corps of Engineers. The pink, blue, yellow, and orange areas are HEC-RAS flood extent corresponding to specific discharge measurements for demonstration purposes.

The geo-topo datasets used in this study include two DEMs and a Height Above the Nearest Drainage (HAND) layer. HAND is widely used for flood extent generation due to its limited requirements for data and computation (Li et al., 2023). We used the slope derived from the 3DEP DEM in post-processing to create the original flood extent, while the topobathy DEM was used for DEM quantile computation during the QFR's filling step. The reason for using two DEMs is that the topobathy DEM only covers limited bank areas close to the river channel and is

not available for the entire study area. Nevertheless, the topobathy was used in HEC-RAS simulation. Therefore, we believe it is reasonable to apply a DEM with full coverage (3DEP DEM in our case) in post-processing while using the topobathy DEM to derive DEM quantiles. HAND, as a normalized elevation denoting the elevation difference between any hillslope pixel and its nearest drainage pixel in drainage networks, indicates how prone a hillslope pixel is to flood (or how vertically close a pixel is to areas that are often flooded) (Nobre et al., 2011; Rennó et al., 2008). HAND was involved in several places throughout the entire workflow as a filling/filtering index. Specifically, it was used as a filter before the original extent was generated; then the quantile of HAND values for all flooded pixels was computed to be used in the filling step; finally, we refined the flood extent using HAND again before the levee step (see also details about QFR procedures in subsection 2.3.2).

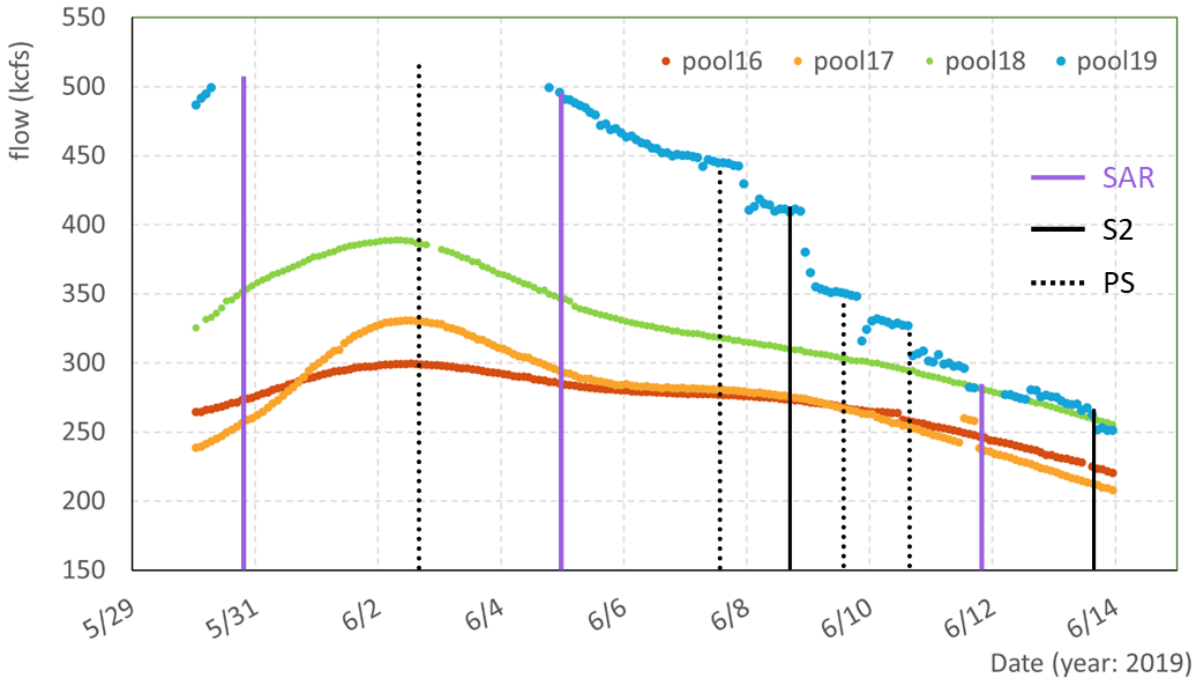

Figure 2. Streamflow of the four pools and RS images availability over the study period. Dots represent streamflow measurements and vertical lines represent the time SAR, S2, or PS images were obtained.

The National Weather Service North Central River Forecast Center provided streamflow measurements of the four sites over the study period. Discharge readings for Pools 16, 17, and 18 were provided every other hour and those for Pool 19 were provided every 15 minutes. Figure 2 depicted the streamflow (shown in dots) measured at those four sites over the study period as well as the time SAR, S2, and PS images were captured (shown in vertical lines). Theoretically, PS images come out at a daily frequency (Sadeh et al., 2021). In practical applications, however, due to cloud contamination, the available images are often limited. This also applies to S2 images. Originally, there was another S2 image captured on June 3, but we have to discard it due

to the limited clear areas not affected by clouds. SAR signals can penetrate clouds and haze and are thus very popular in water resources management applications, especially flood mapping (Ling et al., 2021; Rahman & Thakur, 2018). However, as we can see from Figure 2, a big shortcoming of SAR images is the revisit frequency. In our study area, they are obtained at a 12-day revisit period (which can be comprehended as the interval between two shots of the same region). We got three SAR images because the one obtained on June 5 came from a different orbit, namely, the scope of it did not entirely overlap with the other two but covered some of our study areas. Note that there are some gaps for streamflow data at Pool 19 from about May 30 to June 4 as shown in Figure 2.

The reference maps used in this study generated by the Iowa Flood Center's (IFC) statewide flood mapping project (Gilles et al., 2012) to support better informed decisions for flood preparedness (Yildirim and Demir, 2022), mitigation (Alabbad et al., 2022) and response. The project provided HEC-RAS simulated flood maps following Federal Emergency Management Agency (FEMA) quality guidelines for specific return periods (e.g., 100-yr and 500-yr) as well as maps corresponding to small increments of river stage or streamflow reading (e.g., every 0.5-foot increase in stage or every 10,000 cubic feet per second increase in discharge). The resolution of reference maps is 20 m. All RS-based maps will be resampled to 20 m to allow comparison. Note that resampling was only done before comparison, the original resolution of SAR, S2, and PS remained unchanged for better accuracy during all previous procedures.

Table 1. Dataset source and details used in this study

Item	**Spatial Resolution**	**Collection Date (2019)**	**Sources**
Sentinel-1 GRD Imagery[G]	10 m	05/30, 06/05, 06/11	ESA
Sentinel-2 MSI Surface Reflectance, Level-2A[G]	10 m	06/08, 06/13	ESA
PlanetScope PSScene Surface Reflectance[N]	3 m	06/02, 06/07, 06/09, 06/10	Planet Labs (free of access for non-commercial use through ESA's Earthnet Programme)
Streamflow measurements	-	05/30 ~ 06/13	National Weather Service North Central River Forecast Center
USGS 3DEP DEM[G]	10 m	-	USGS
Upper Mississippi River System Topobathy	Resampled from 2m to 10m	-	U.S. Army Corps of Engineers (USACE, 2016)
HAND[O]	10 m	-	Height Above Nearest Drainage (HAND) for CONUS (Liu, 2018)

G: Data that are openly available on and pulled directly from Google Earth Engine platform
O: Data that are openly available online
N: Data that are normalized to Sentinel-2 bands for consistent radiometry

2.3. Methodology

2.3.1. Matching RS Imagery with Streamflow Measurement and Reference Maps

To ensure the RS-based flood maps and the reference match each other, we first determine the streamflow by matching the capture time of the RS images with the time the streamflow was measured based on the selected flood event (Haltas et al., 2021). Then, the reference map that corresponds to that specific streamflow was selected for comparison. It is worth noting that although the time each RS image was captured was not depicted in Figure 2 and was not listed in Table 1, the time used for matching between images and streamflow measurements is accurate to the minute. For instance, the SAR image on May 30 was captured at 23:57 pm UTC, thus the appropriate streamflow to use is the one that was obtained at about the same time. Admittedly, sometimes, there are unavoidable mismatches in the time. For instance, streamflow was measured at 23:00 pm May 30 and 1:00 am May 31, but the image was at 23:57 pm May 30. Also, there may not be a reference map that exactly matches the streamflow selected (e.g., the streamflow is 326,700 cfs and the closest reference maps are for 320,000 and 330,000 cfs). In those cases, we adopted the temporally closest streamflow and the reference map corresponding to streamflow that is the closest numerically.

2.3.2. RS-Based Flood Mapping with QFR Procedures

The whole process started with RS image pre-processing. For SAR images, we first mosaiced images as needed. The images obtained on May 30 and June 11 each consist of two consecutive images of one scan, whereas the one obtained on June 5 contains only one image. We then denoised images with a 7×7 Refined Lee filter. For the two optical imageries, we first removed cloud and cloud shadow. For S2, we used CSD-SI method without temporal median adjustment (Zhai et al., 2018). For PS, unclear pixels were filtered out using the clear map of the Usable Data Mask 2 (UDM2) assets that came along with PS scenes. Then, the Normalized Difference Water Index (NDWI) was computed using the Green and Near Infrared bands. Note that the NDWI of S2 and PS are computed separately. The two arrows pointing to the NDWI box in Figure 3 were only to avoid redundancy and not mean any interaction between S2 and PS images. Bmax Otsu thresholding was then applied to images done with pre-processing to obtain the rudimentary flood extent. Bmax Otsu method was proposed by Cao et al. (2019) to deal with situations where the bimodal assumption of the original Otsu is not met considering the study region as a whole. Bmax Otsu applied a chessboard segmentation and check the bimodality within each subregion (Markert et al., 2020). For subregions where bimodality is satisfied, Otsu thresholding is applied to classify pixels into foreground and background (or flooded and dry). We then applied a few post-processing steps to remove false-positive (pixels that are classified as flooded but should be dry) pixels with some commonly used geo-topo indexes in RS-based flood mapping applications (Tsyganskaya et al., 2016, 2018). We recommend moderate adjustment of those indexes in order to get satisfying results for different regions.

In most situations where inundated areas are not covered by dense vegetation or other objects that block the view of satellites, the above procedures should be enough to get satisfying flood

maps. In our case, however, after analyzing RS imagery, the derived flood maps, and HEC-RAS reference maps, we discovered that some of our study area is blocked by dense crown canopy, which therefore led to noticeable false-negative areas (classified as dry but should be flooded), for both optical and C-band SAR sensors are unable to see through dense vegetation. One solution is to use images with bands that have a longer wavelength (NASA, n.d.; Refice et al., 2020), such as L-band signals. The drawback is that those images are far less supported on third-party open platforms, such as GEE, and thus require more processing efforts and local computational resources. Furthermore, replacing the triple-sourced imagery with a single-sourced one means less data to use. Given the purpose of this study (continuously mapping water extent over the study period), we believe that correcting the obtained flood extent is the more appropriate approach.

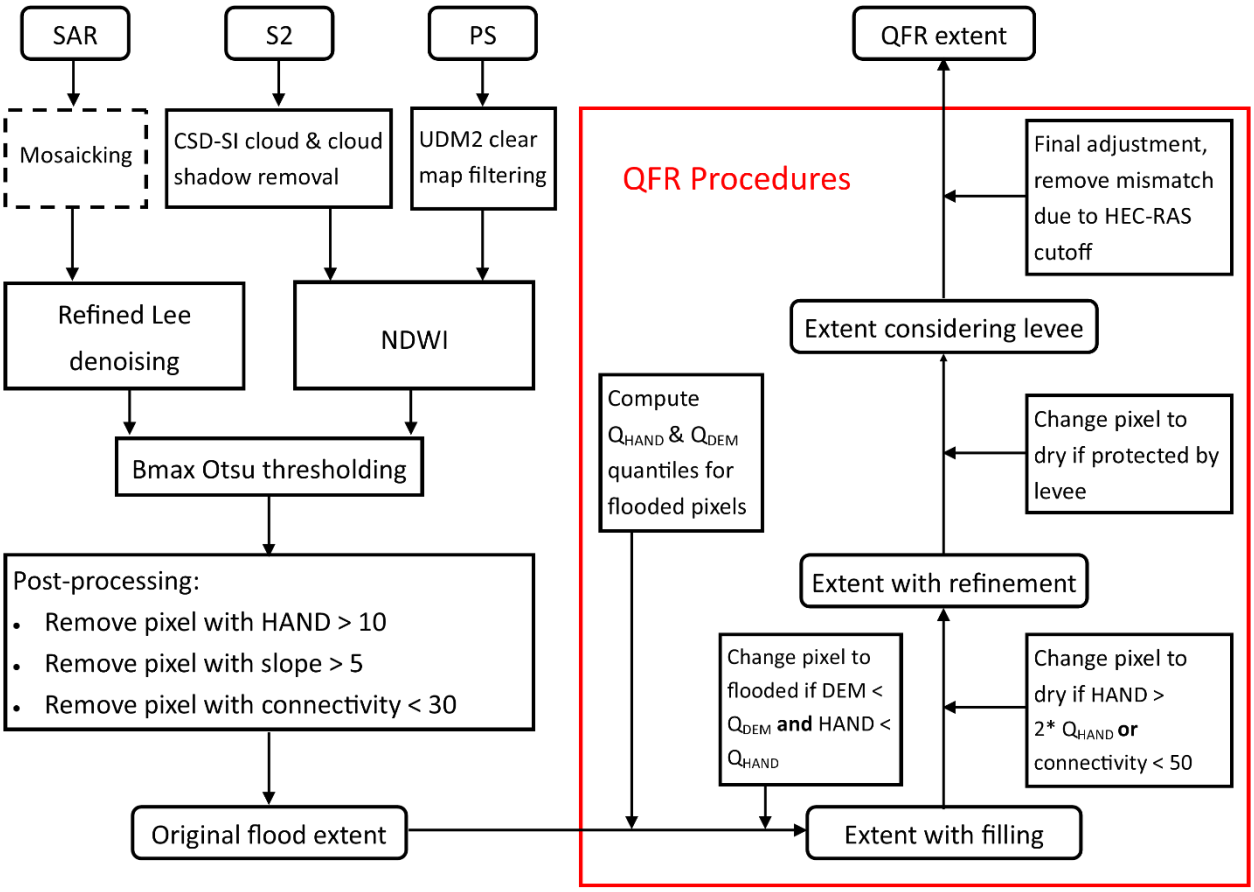

Figure 3. Workflow of RS-based flood mapping with QFR procedures.

QFR procedures shown in Figure 3 are introduced for correcting the flood extent and to recover areas that are misclassified due to the blocking effect of vegetation. The QFR starts with computing the quantiles of HAND and DEM for flooded pixels on the original flood map. Then, the filling process changed the dry pixels to flooded if their HAND and DEM values are smaller than the two quantiles. Then, the refining process removes incorrect flooded pixels by screening with HAND and connectivity again. Next, pixels that are in flooded areas protected by levees

were changed to dry. The levee step should only be used when levees exist. The justification of this step is that areas protected by levees often have low elevations and are close to river networks, which means those are highly likely to be inundated without levees, in other words, to be determined flooded during the filling step. Thus, the levee step simulates the effect of having levees around the protected areas. Finally, the flood extent was slightly adjusted for comparison. This is because of the artificial cutoff of HEC-RAS maps. HEC-RAS was run for each of the four pools shown in Figure 1 and thus contains manual cutoffs around the starting and ending positions of each river segment. As our RS-based maps are derived for the entire study area, it is necessary to 'simulate' those cutoffs so that pixels on the RS maps that are beyond the region of each HEC-RAS simulation will not be counted as mismatches in comparison.

2.3.3. Flood Map Evaluation

We adopted both qualitative and quantitative approaches to evaluate RS-based flood maps by comparing them with HEC-RAS flood maps. For qualitative evaluations, we visualized RS flood maps, including RS maps at different QFR processing steps, original RS imagery, and reference maps to allow easy visual comparison.

For quantitative analysis, we adopted Accuracy (A), Hit Rate (H), Kappa value (K), and Fitness-Statistic (F) to evaluate the consistency between RS flood maps and reference maps. A value measures the ratio of correct predictions versus all predictions made by a model. It ranges between 0 and 1 with 1 being the best possible value. A value is calculated as follows:

$$A = \frac{TP + TN}{TP + FN + FP + TN} \tag{1}$$

TP, TN, FP, and FN are the four statuses of a prediction compared to the truth or the reference, where T (True) indicates the prediction is consistent with the truth, F (False) indicates the prediction is different from the truth, P (Positive) means the model determines a pixel to be flooded, and N (Negative) means a pixel being dry according to the model.

H is the ratio of correct positive (flooded) predictions versus all positive predictions made by the model. H has the same range as A value and also has 1 as its best value. H value is calculated as follows:

$$H = \frac{TP}{TP + FN} \tag{2}$$

K and F (also known as Critical Success Index, CSI) are two complementary indexes with the former focusing more on dry pixels and the latter focusing more on flooded pixels (Afshari et al., 2018). The best possible value for both K and F is 1. K and F is calculated as follow:

$$K = \frac{N(TP + TN) - \big((TP + FP) \times (TP + FN) + (FP + TN) \times (FN + TN)\big)}{N^2 - \big((TP + FP) \times (TP + FN) + (FP + TN) \times (FN + TN)\big)} \tag{3}$$

$$F = \frac{TP}{TP + FN + FP} \quad (4)$$

3. Results and Discussion

Table 2 compares two RS maps (the original flood extent without QFR processes and the QFR extent) with HEC-RAS maps. As shown in Table 2, the QFR extent is noticeably improved over the original extent, proving the efficacy of the QFR workflow in resolving the blocking effect of dense vegetation. We also noticed that the original extent of Pool 17 is the worst among all four sites. Its F and K values are still worse than the other three sites after QFR, whereas the H value has been dramatically improved. The second worse performance after QFR occurred in the Pool 19 area, with all three indexes slightly worse than those in Pool 16 and Pool 18 areas. After analyzing the RGB RS images, the RS flood maps, and the HEC-RAS maps, we discovered that the relatively worse performance of QFR in Pools 17 and 19 were due to errors in HEC-RAS maps and not errors in RS maps. We will explain it with examples later in this section when discussing Figures 7 and 8.

Table 2. The consistency of the RS-based flood extent evaluated against HEC-RAS simulation. The original indexes are averaged results of the original flood extent without QFR.

Gauge No.	Average H QFR (%)	Average H Original (%)	Average F QFR (%)	Average F Original (%)	Average QFR K (%)	Average K Original (%)
Pool16	87.13	59.78	77.42	46.12	84.01	54.44
Pool17	91.21	53.73	71.98	24.75	79.89	19.46
Pool18	87.46	58.08	77.38	33.71	83.45	29.77
Pool19	82.48	59.70	72.28	34.73	81.09	41.35

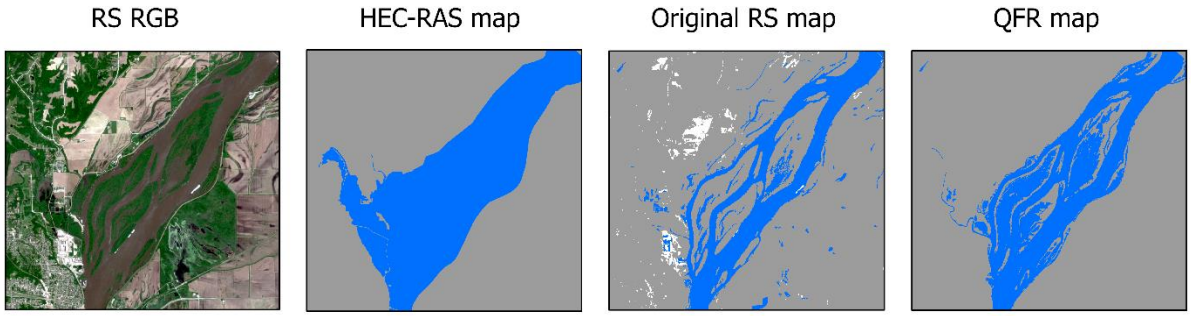

Figure 4. One example to demonstrate the necessity of QFR in this study with a segment within the Pool 19 area. Gray areas are dry whereas blue areas are flooded. The RS RGB is an S2 image, with the white areas masked due to cloud coverage and other quality issues.

Figure 4 depicts a segment in Pool 19 area with a large portion of flooded areas blocked by dense vegetation and thus necessitated QFR. As we can see from the original RS flood extent in Figure 4, Bmax Otsu thresholding and post-processing can successfully identify open flooded areas and dry areas but failed to work well in other areas. A close investigation of the RS image

revealed that the areas inside the river should be inundated, just as shown in the HEC-RAS map, as one can find flood water occurred in the gaps of the vegetation by enlarging the image. Since the vegetation are spatially adjacent and the surface underneath is highly likely to have similar geo-statuses, such as similar elevation, it is thus of great possibility that there is flood covering the entire river segment (including those under dense vegetation). The QFR map of Figure 4 shows noticeable improvement compared to the original RS map. Nevertheless, we also see that there are still some areas not corrected by QFR procedures.

Figure 5 is the box plot showing the accuracy of RS flood maps at different processing stages. It is clear that as QFR proceeded (original extent -› extent with filling and refinement -› extent considering levees -› extent with final adjustments), the consistency between RS flood maps and HEC-RAS maps improves, regardless of the RS sources. Note that Figure 5 (b) plots the results after the filling and the refining step, not only out of figure layout considerations but, more importantly, due to the fact that the filling step introduces far more changes than the refining step (see also Figure 6 for visualizations of maps after these two steps).

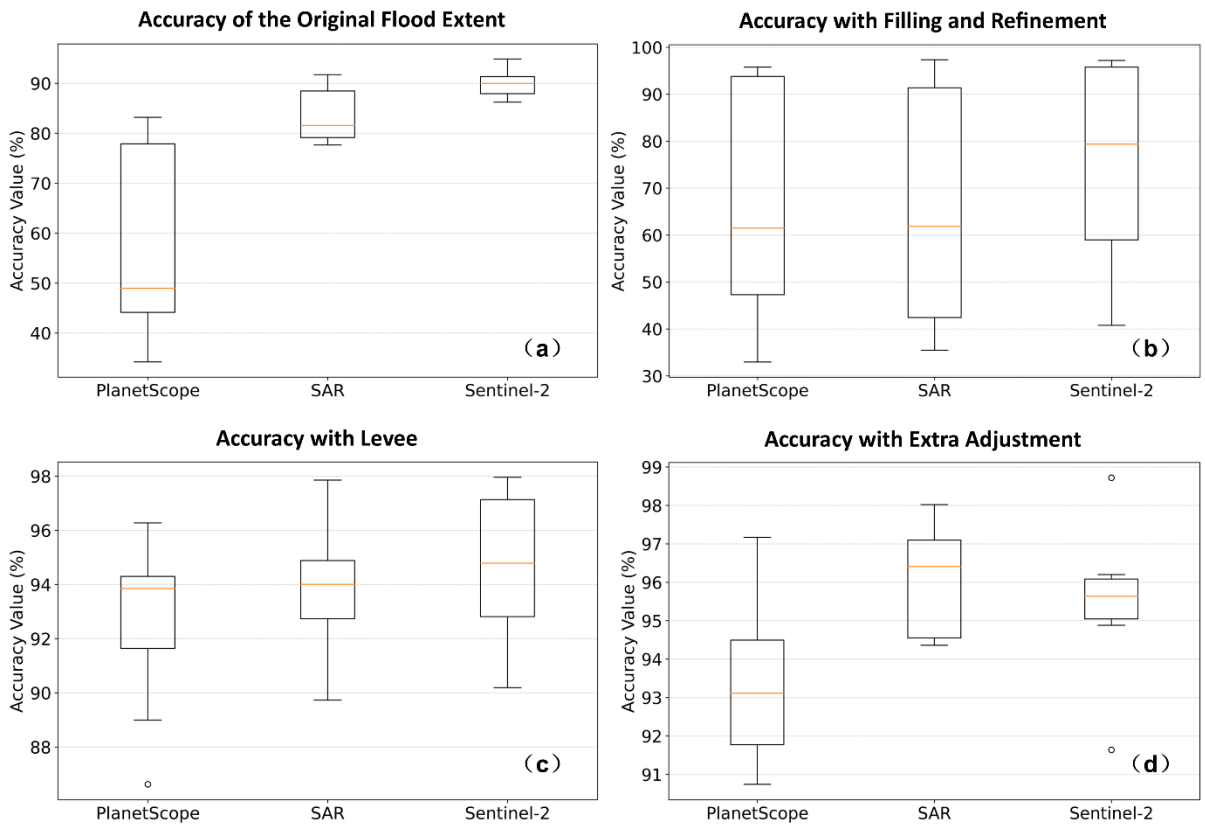

Figure 5. Boxplots of RS-based flood extent validated against HEC-RAS simulation. a) results of extent that did not go through any QFR processes; b) results of extent that went through filling and refinement; c) results of extent that further considered the influence of levee; d) results of extent that were further adjusted considering the artificial cutoff and obvious mismatches.

Therefore, doing a separate plot for refining is unnecessary. We also noticed that the accuracy of the original and QFR extent derived from SAR is comparable with S2. They both are better than those from PS, especially for the original maps. Maps processed with steps in the middle (Figure 5 (b) and (c)) do not show significant differences. Nevertheless, results from S2 are still better than those from SAR and PS. Figure 5 clearly shows the efficacy of QFR in solving the blocking effect from dense vegetation. It also demonstrates the superiority of S2 and SAR over PS images.

PlanetScope miniature satellite constellation is able to provide 3m spatial resolution and 1-day temporal resolution multispectral optical earth surface observations. Its improved spatial and temporal resolution over many commonly used RS imageries (e.g., Landsat, Sentinel-2, SAR, and MODIS) have boosted its popularity in multiple aspects, including surface water extent mapping, over the recent years. However, lack of on-board calibration (Huang & Roy, 2021) as well as the difference between sensors of different generations made images from PlanetScope less consistent compared to image series from other platforms such as Landsat and Sentinel-2 (Frazier & Hemingway, 2021; Huang & Roy, 2021).

Our results are consistent with previous findings about the quality of PlanetScope images. Specifically, we found that there were two major issues with PS imagery. One is the radiometric discrepancy between images. The discrepancy not only existed in sensors of different generations, but also between images captured by the sensors of the same generation and even images captured by the same sensor a few minutes apart. Those discrepancies greatly increased the image pre-processing time and effort. The radiometric discrepancy between PS imagery and S2 imagery is another big issue. Although we used the built-in function provided by Planet Labs to harmonize PS data with Copernicus Sentinel-2 images when exporting PS images, it did not help much.

The above two reasons led to not only noticeable visual differences between the PS and S2 images used in this study, but also have quantitative influence. The NDWI index was proved useful in water extent extraction by many previous studies (Cavallo et al., 2021; Goffi et al., 2020; Thapa et al., 2022). The threshold is theoretically set around 0, with values greater than 0 being flooded areas. In practice, the threshold may vary slightly among different study regions (Tulbure et al., 2022). The Bmax Otsu algorithm automatically determined the optical NDWI threshold for S2 images used in this study to be around -0.2 whereas being around -0.6 for PS. The small NDWI threshold for PS directly resulted in large false flooded areas in the original extent map as shown in Figure 6, where a large portion of dry areas shown in the RGB sub-plot were determined inundated.

Fortunately, the QFR procedures successfully removed most of the wrong predictions due to PS image quality issues discussed above and made the final flood extent far more consistent with the reference compared to the original stage as shown in Figure 6. Because the original PS-derived extent tends to overestimate a lot, we found smaller quantiles (3/4 and 7/8) worked the best in most cases in the filling step of QFR for PS images. For SAR and S2, as expected, the optimal quantiles are slightly larger and are about 7/8 and 15/16.

Based on those findings, we believe that PS imagery should be used with extra care, especially for multi-spatial and multi-temporal where it is more likely to involve images captured by different sensors, including sensors of the same generation and sensors of different generations.

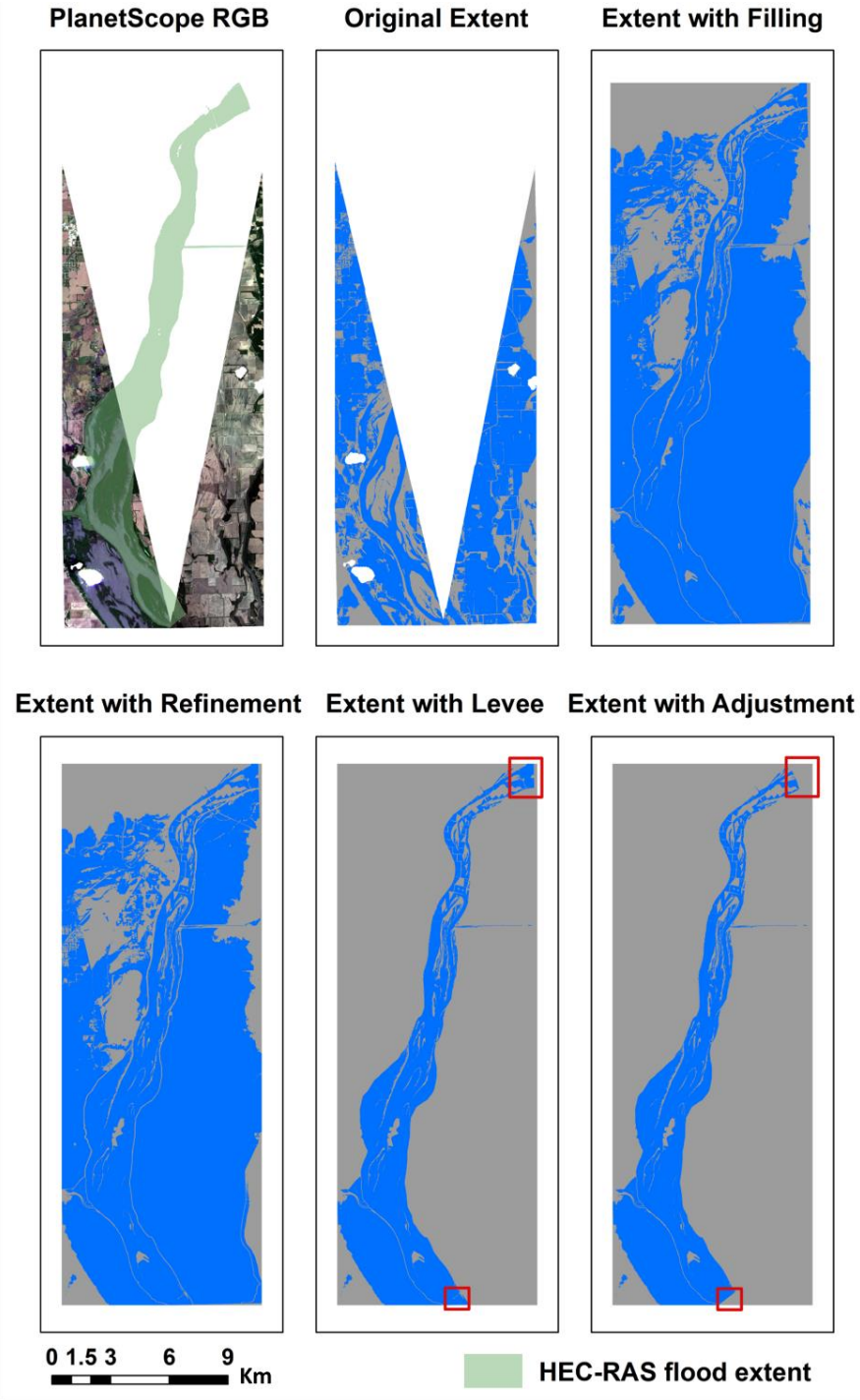

Figure 6. The original flood extent derived from PlanetScope imagery on June 10, 2019, and the extent after each procedure of QFR. Gray areas are dry whereas blue areas are flooded. The four red boxes are locations where artificial cutoff of HEC-RAS flood extent occurred.

As discussed at the beginning of this section, we mentioned that the worse consistency of RS-based maps in Pool 17 and Pool 19 areas was due to the error of HEC-RAS predictions rather than RS predictions. Two examples for Pool 17 and Pool 19 were given to demonstrate the difference between the two predictions. As shown in Figure 7, the major discrepancy between HEC-RAS and QFR maps occurred in the red box at the bottom. The RGB image clearly shows that HEC-RAS missed a flooded region in the lower-left corner. Similarly, HEC-RAS overestimated a non-negligible area in the middle of the river segment observed on June 8 in Pool 19 area. The Sentinel-2 RGB of Figure 8 clearly shows that the over-predicted area by HEC-RAS in the red box is dry. Those errors in Pool 17 and Pool 19 areas repeated on reference maps corresponding to a few different streamflow conditions, and thus increased the overall discrepancy between HEC-RAS and QFR maps in those two areas.

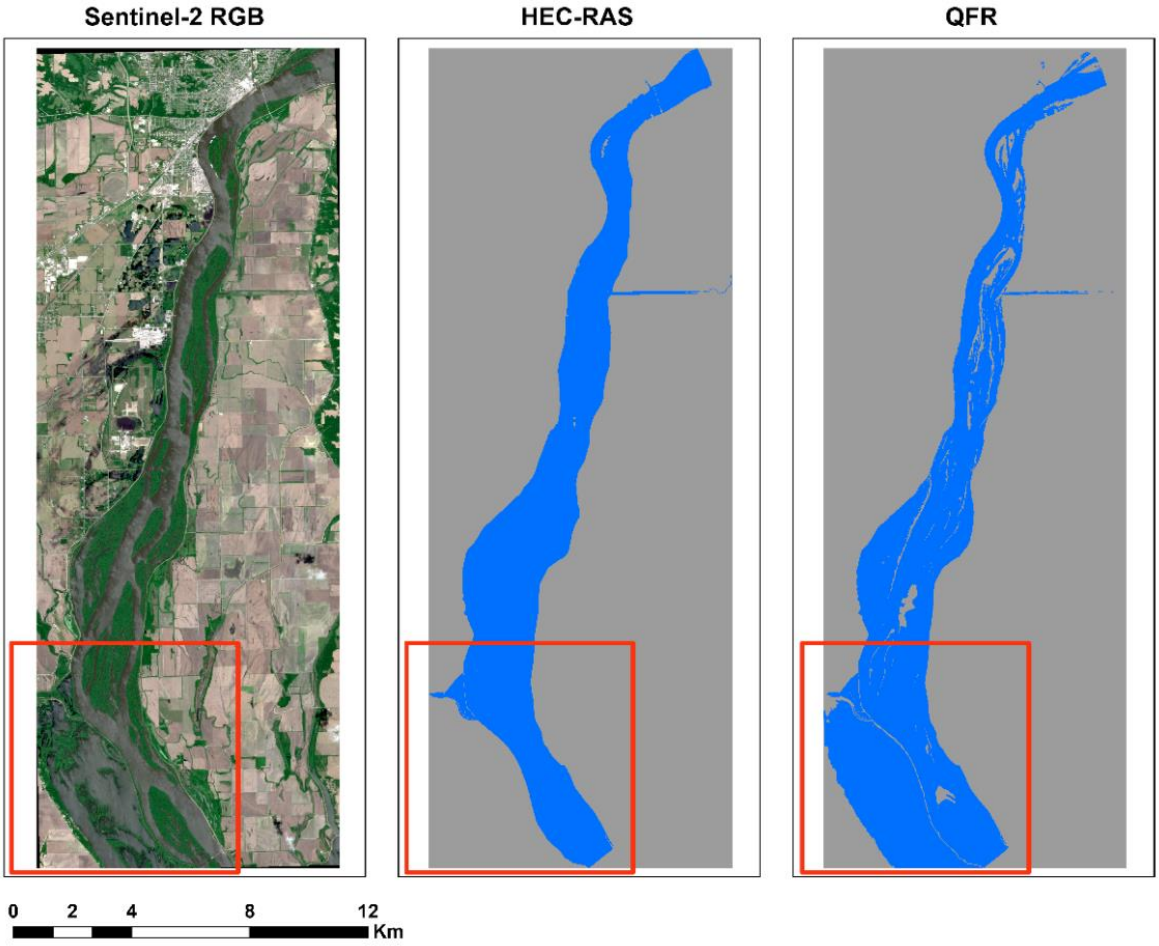

Figure 7. The QFR flood extent derived from Sentinel-2 imagery on June 13, 2019, and the corresponding HEC-RAS simulation at Pool 17 location. Gray areas are dry whereas blue areas are flooded.

Despite some of those errors mentioned above, we still believe HEC-RAS is useful, as most of its predictions are reasonable and consistent with RS conditions. Based on our findings, we

recommend using HEC-RAS with a bit more care, especially in regions with complex hydro-conditions. Additionally, extra validation, if available, will also be helpful.

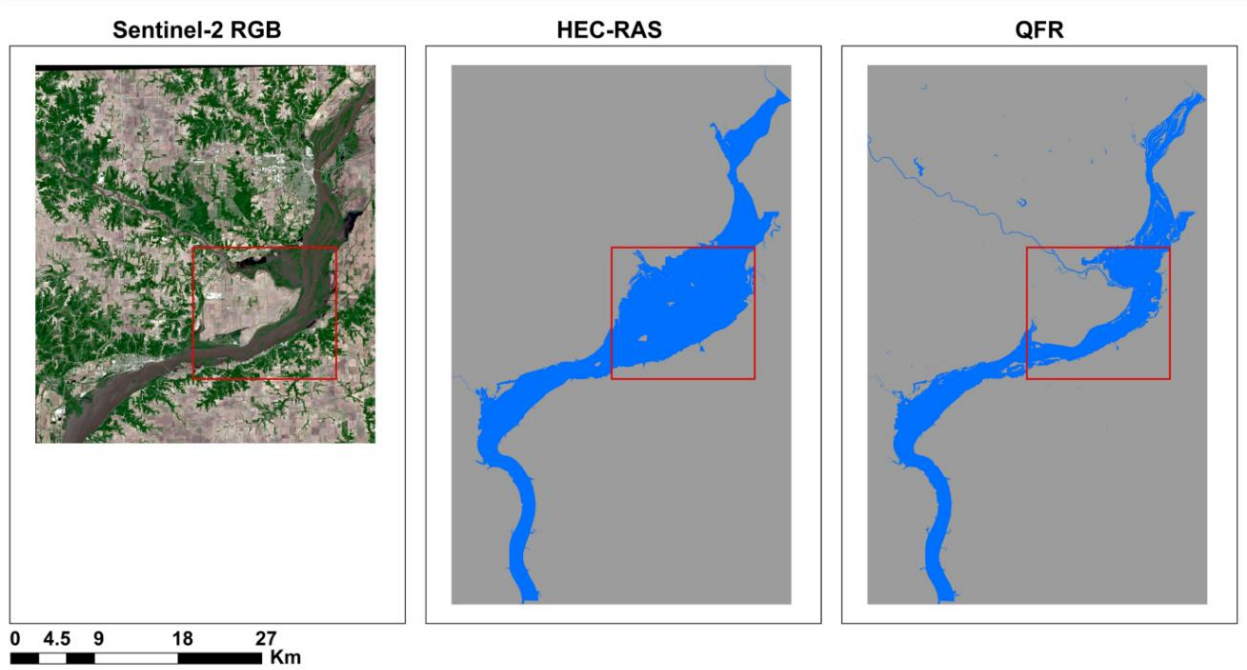

Figure 8. The QFR flood extent derived from Sentinel-2 imagery on June 8, 2019, and the corresponding HEC-RAS simulation at Pool 19 location. Gray areas are dry whereas blue areas are flooded.

4. Conclusion

This study proposed a workflow that extracts surface water extent and incorporates Quantile-based Filling & Refining (QFR) procedures to resolve the blocking effect of dense vegetation on water extent derived from multimodal remote sensing (RS) images, given the RS signals are not able to penetrate the crown canopy. We test the proposed workflow with the flooding that occurred in the Mississippi River segments at Locks and Dams 16, 17, 18, and 19 from May 30 to June 13, 2019. We evaluated the flood maps w/ and w/o QFR, and maps that were done with some QFR steps against HEC-RAS flood maps. We followed the chain rule of "image capture time—streamflow measuring time—corresponding streamflow—corresponding HEC-RAS map" to locate the correct reference.

Due to the blocking effect of crown canopies, the flood maps not processed with QFR were greatly underestimated with lots of inundated areas in HEC-RAS maps not identified. In contrast, QFR maps showed substantial agreement with HEC-RAS maps with noticeable improvements. Considering the four sites altogether, the H, F, and K values of QFR maps improved by 50.1%, 114.7%, and 126.5%, respectively, compared to the original maps without QFR. Results also showed that each step of QFR, namely, the Filling, Refining, and Levee, has its own impact and all contribute to performance improvement. While the filling and refining steps can be applied

universally, we do argue that the levee step, where the protecting effect of levees is considered, should be applied when there are levees exist.

Despite often being used as "ground truth" with the absence or insufficiency of real ground observations, HEC-RAS simulations are not perfect. The error in HEC-RAS maps led to a larger discrepancy between those maps and RS-based flood extent in Pools 17 and 19 in our study. We thus recommend the combined use of HEC-RAS and other independent data sources for reference purposes to avoid errors that may occur.

Finally, consistent with findings of previous studies in the literature, our results showed that PlanetScope imageries, due to the discrepancy between different satellites and lacking on-board calibration, did not guarantee consistent radiometry between different images or when compared to Sentinel-2 imagery. The built-in harmonization function provided by Planet Lab before exporting images from the platform did not help much with the inconsistency. Given that, we recommend that PlanetScope images should be used with extra care and are suitable for small-scale (both temporally and spatially) analysis to avoid large discrepancies between images unless the radiometry can be effectively harmonized over all images to be used.

The proposed QFR procedures are simple but proven effective, and thus have the potential to be adopted into automatic flood mapping programs to benefit near-real-time flood inundation mapping and decision support applications. Incorporating the QFR into some of the most widely used geospatial/RS analyzing platforms, such as GEE, and adopting the QFR for near-real-time RS-based flood extent mapping are future research topics that are worth exploring.

Acknowledgement

We would like to acknowledge the National Weather Service North Central River Forecast Center for providing streamflow measurements and Iowa Flood Center for providing HEC-RAS flood maps for comparison and providing access to PlanetScope imagery.

Reference

Afshari, S., Tavakoly, A. A., Rajib, M. A., Zheng, X., Follum, M. L., Omranian, E., & Fekete, B. M. (2018). Comparison of new generation low-complexity flood inundation mapping tools with a hydrodynamic model. Journal of Hydrology, 556, 539–556. https://doi.org/10.1016/j.jhydrol.2017.11.036

Alabbad, Y., & Demir, I. (2022). Comprehensive flood vulnerability analysis in urban communities: Iowa case study. International journal of disaster risk reduction, 74, 102955.

Alabbad, Y., Yildirim, E., & Demir, I. (2022). Flood mitigation data analytics and decision support framework: Iowa Middle Cedar Watershed case study. Science of The Total Environment, 814, 152768.

Ali, A. U., & Ogie, R. (2017). Social media and disasters: Highlighting some wicked problems. IEEE Technology and Society Magazine, 36(4). https://doi.org/10.1109/MTS.2017.2763450

Anusha, N., & Bharathi, B. (2020). Flood detection and flood mapping using multi-temporal synthetic aperture radar and optical data. The Egyptian Journal of Remote Sensing and Space Science, 23(2), 207–219. https://doi.org/10.1016/J.EJRS.2019.01.001

Avand, M., Moradi, H., & lasboyee, M. R. (2021). Using machine learning models, remote sensing, and GIS to investigate the effects of changing climates and land uses on flood probability. Journal of Hydrology, 595, 125663. https://doi.org/10.1016/J.JHYDROL.2020.125663

Billah, M., Islam, A. K. M. S., Mamoon, W. Bin, & Rahman, M. R. (2023). Random forest classifications for landuse mapping to assess rapid flood damage using Sentinel-1 and Sentinel-2 data. Remote Sensing Applications: Society and Environment, 30, 100947. https://doi.org/10.1016/J.RSASE.2023.100947

Cao, H., Zhang, H., Wang, C., Water, B. Z.-, & 2019, undefined. (2019). Operational flood detection using Sentinel-1 SAR data over large areas. Water, 11(4). https://doi.org/10.3390/w11040786

Cavallo, C., Papa, M. N., Gargiulo, M., Palau-Salvador, G., Vezza, P., & Ruello, G. (2021). Continuous Monitoring of the Flooding Dynamics in the Albufera Wetland (Spain) by Landsat-8 and Sentinel-2 Datasets. Remote Sensing 2021, Vol. 13, Page 3525, 13(17), 3525. https://doi.org/10.3390/RS13173525

Costache, R., Pham, Q. B., Corodescu-Roşca, E., Cîmpianu, C., Hong, H., Thuy Linh, N. T., Fai, C. M., Ahmed, A. N., Vojtek, M., Pandhiani, S. M., Minea, G., Ciobotaru, N., Popa, M. C., Diaconu, D. C., & Pham, B. T. (2020). Using GIS, Remote Sensing, and Machine Learning to Highlight the Correlation between the Land-Use/Land-Cover Changes and Flash-Flood Potential. Remote Sensing 2020, Vol. 12, Page 1422, 12(9), 1422. https://doi.org/10.3390/RS12091422

Costache, R., Pham, Q. B., Sharifi, E., Linh, N. T. T., Abba, S. I., Vojtek, M., Vojteková, J., Nhi, P. T. T., & Khoi, D. N. (2019). Flash-Flood Susceptibility Assessment Using Multi-Criteria Decision Making and Machine Learning Supported by Remote Sensing and GIS Techniques. Remote Sensing 2020, Vol. 12, Page 106, 12(1), 106. https://doi.org/10.3390/RS12010106

Dalla Mura, M., Prasad, S., Pacifici, F., Gamba, P., Chanussot, J., & Benediktsson, J. A. (2015). Challenges and Opportunities of Multimodality and Data Fusion in Remote Sensing. Proceedings of the IEEE, 103(9), 1585–1601. https://doi.org/10.1109/JPROC.2015.2462751

Demir, I., Conover, H., Krajewski, W.F., Seo, B.C., Goska, R., He, Y., McEniry, M.F., Graves, S.J. and Petersen, W., (2015). Data-enabled field experiment planning, management, and research using cyberinfrastructure. Journal of Hydrometeorology, 16(3), pp.1155-1170.

Frazier, A. E., & Hemingway, B. L. (2021). A Technical Review of Planet Smallsat Data: Practical Considerations for Processing and Using PlanetScope Imagery. Remote Sensing 2021, Vol. 13, Page 3930, 13(19), 3930. https://doi.org/10.3390/RS13193930

Gao, W., Shen, Q., Zhou, Y., & Li, X. (2018). Analysis of flood inundation in ungauged basins based on multi-source remote sensing data. Environmental Monitoring and Assessment, 190(3), 1–13. https://doi.org/10.1007/S10661-018-6499-4/METRICS

Gašparovič, M., & Klobučar, D. (2021). Mapping Floods in Lowland Forest Using Sentinel-1 and Sentinel-2 Data and an Object-Based Approach. Forests 2021, Vol. 12, Page 553, 12(5), 553. https://doi.org/10.3390/F12050553

Gautam, A., Sit, M., & Demir, I. (2022). Realistic river image synthesis using deep generative adversarial networks. Frontiers in water, 4, 10.

Gilles, D., Young, N., Schroeder, H., Piotrowski, J., & Chang, Y. J. (2012). Inundation mapping initiatives of the iowa flood center: Statewide coverage and detailed urban flooding analysis. Water (Switzerland), 4(1), 85–106. https://doi.org/10.3390/w4010085

Goffi, A., Stroppiana, D., Brivio, P. A., Bordogna, G., & Boschetti, M. (2020). Towards an automated approach to map flooded areas from Sentinel-2 MSI data and soft integration of water spectral features. International Journal of Applied Earth Observation and Geoinformation, 84, 101951. https://doi.org/10.1016/J.JAG.2019.101951

Haltas, I., Yildirim, E., Oztas, F., & Demir, I. (2021). A comprehensive flood event specification and inventory: 1930–2020 Turkey case study. International Journal of Disaster Risk Reduction, 56, 102086.

He, W., & Yokoya, N. (2018). Multi-Temporal Sentinel-1 and -2 Data Fusion for Optical Image Simulation. ISPRS International Journal of Geo-Information 2018, Vol. 7, Page 389, 7(10), 389. https://doi.org/10.3390/IJGI7100389

Hu, A., & Demir, I. (2021). Real-time flood mapping on client-side web systems using hand model. Hydrology, 8(2), 65.

Hu, J., Liu, R., Hong, D., Camero, A., Yao, J., Schneider, M., Kurz, F., Segl, K., & Zhu, X. X. (2023). MDAS: a new multimodal benchmark dataset for remote sensing. Earth System Science Data, 15(1), 113–131. https://doi.org/10.5194/ESSD-15-113-2023

Huang, H., & Roy, D. P. (2021). Characterization of Planetscope-0 Planetscope-1 surface reflectance and normalized difference vegetation index continuity. Science of Remote Sensing, 3, 100014. https://doi.org/10.1016/J.SRS.2021.100014

Islam, K. A., Uddin, M. S., Kwan, C., & Li, J. (2020). Flood Detection Using Multi-Modal and Multi-Temporal Images: A Comparative Study. Remote Sensing 2020, Vol. 12, Page 2455, 12(15), 2455. https://doi.org/10.3390/RS12152455

Jiang, M., Shen, H., & Li, J. (2022). Deep-Learning-Based Spatio-Temporal-Spectral Integrated Fusion of Heterogeneous Remote Sensing Images. IEEE Transactions on Geoscience and Remote Sensing, 60. https://doi.org/10.1109/TGRS.2022.3188998

Kim, J. G., Kang, B., & Kim, S. (2022). Flood Inflow Estimation in an Ungauged Simple Serial Cascade of Reservoir System Using Sentinel-2 Multi-Spectral Imageries: A Case Study of Imjin River, South Korea. Remote Sensing 2022, Vol. 14, Page 3699, 14(15), 3699. https://doi.org/10.3390/RS14153699

Li, Z., Wang, C., Emrich, C. T., & Guo, D. (2018). A novel approach to leveraging social media for rapid flood mapping: a case study of the 2015 South Carolina floods. Cartography and Geographic Information Science, 45(2), 97–110. https://doi.org/10.1080/15230406.2016.1271356

Li, Z., & Demir, I. (2023a). U-net-based semantic classification for flood extent extraction using SAR imagery and GEE platform: A case study for 2019 central US flooding. Science of The Total Environment, 869, 161757.

Li, Z., & Demir, I. (2023b). Better Localized Predictions with Out-of-Scope Information and Explainable AI: One-Shot SAR Backscatter Nowcast Framework with Data from Neighboring Region. EarthArxiv, 5509. https://doi.org/10.31223/X5P95M

Li, Z., & Demir, I. (2022). A comprehensive web-based system for flood inundation map generation and comparative analysis based on height above nearest drainage. Science of The Total Environment, 828, 154420.

Li, Z., Mount, J., & Demir, I. (2022a). Accounting for uncertainty in real-time flood inundation mapping using HAND model: Iowa case study. Natural Hazards, 112(1), 977-1004.

Li, Z., Xiang, Z., Demiray, B. Z., Sit, M., & Demir, I. (2022b). MA-SARNet: A One-Shot Forecasting Framework for SAR Image Prediction with Physical Driving Forces. EarthArxiv, 4846, https://doi.org/10.31223/X5765J

Li, Z., Duque, F. Q., Grout, T., Bates, B., & Demir, I. (2023). Comparative analysis of performance and mechanisms of flood inundation map generation using Height Above Nearest Drainage. Environmental Modelling & Software, 159, 105565.

Ling, J., Zhang, H., Lin, Y., Li, X., Guan, X., Feng, R., & Yu, Y. (2021). Improving Urban Land Cover Classification in Cloud-Prone Areas with Polarimetric SAR Images. Remote Sensing 2021, Vol. 13, Page 4708, 13(22), 4708. https://doi.org/10.3390/RS13224708

Liu, Y. (2018). Height Above Nearest Drainage (HAND) for CONUS | CUAHSI HydroShare. https://doi.org/Liu, Y. (2018). Height Above Nearest Drainage (HAND) for CONUS, HydroShare, https://doi.org/10.4211/hs.69f7d237675c4c73938481904358c789

Margareta Wahlstrom, D. G.-S. (2015). The Human Costs of Weather Related Disasters. In The United Nations Office for Diaster Risk Reduction. https://www.unisdr.org/files/46796_cop21weatherdisastersreport2015.pdf

Markert, K. N., Markert, A. M., Mayer, T., Nauman, C., Haag, A., Poortinga, A., Bhandari, B., Thwal, N. S., Kunlamai, T., Chishtie, F., Kwant, M., Phongsapan, K., Clinton, N., Towashiraporn, P., & Saah, D. (2020). Comparing Sentinel-1 surface water mapping algorithms and radiometric terrain correction processing in southeast Asia utilizing Google Earth Engine. Remote Sensing, 12(15), 2469. https://doi.org/10.3390/RS12152469

Martinis, S., Rieke, C., J-P Schumann, G., Balzter, H., & Thenkabail, P. S. (2015). Backscatter Analysis Using Multi-Temporal and Multi-Frequency SAR Data in the Context of Flood Mapping at River Saale, Germany. Remote Sensing 2015, Vol. 7, Pages 7732-7752, 7(6), 7732–7752. https://doi.org/10.3390/RS70607732

Musser, J., Watson, K., Painter, J., & Gotvald, A. (2016). Flood-inundation maps of selected areas affected by the flood of October 2015 in central and coastal South Carolina. https://pubs.er.usgs.gov/publication/ofr20161019

Muste, M., Lyn, D. A., Admiraal, D., Ettema, R., Nikora, V., & García, M. H. (Eds.). (2017). Experimental hydraulics: Methods, instrumentation, data processing and management: Volume I: Fundamentals and methods. CRC Press.

NASA. (n.d.). What is Synthetic Aperture Radar? | Earthdata. Retrieved June 1, 2023, from https://www.earthdata.nasa.gov/learn/backgrounders/what-is-sar

NOAA. (n.d.). Weather Related Fatality and Injury Statistics. NOAA's National Weather Service. Retrieved February 1, 2022, from https://www.weather.gov/hazstat/

Nobre, A. D., Cuartas, L. A., Hodnett, M., Rennó, C. D., Rodrigues, G., Silveira, A., Waterloo, M., & Saleska, S. (2011). Height Above the Nearest Drainage - a hydrologically relevant new terrain model. Journal of Hydrology, 404(1–2), 13–29. https://doi.org/10.1016/j.jhydrol.2011.03.051

Rahman, M. R., & Thakur, P. K. (2018). Detecting, mapping and analysing of flood water propagation using synthetic aperture radar (SAR) satellite data and GIS: A case study from the Kendrapara District of Orissa State of India. The Egyptian Journal of Remote Sensing and Space Science, 21, S37–S41. https://doi.org/10.1016/J.EJRS.2017.10.002

Rambour, C., Audebert, N., Koeniguer, E., Le Saux, B., Crucianu, M., & Datcu, M. (2020). Flood Detection in Time Series of Optical and SAR Images. The International Archives of the Photogrammetry, Remote Sensing and Spatial Information Sciences, XLIII-B2-2020(B2), 1343–1346. https://doi.org/10.5194/ISPRS-ARCHIVES-XLIII-B2-2020-1343-2020

Refice, A., Zingaro, M., D'addabbo, A., & Chini, M. (2020). Integrating C- and L-Band SAR Imagery for Detailed Flood Monitoring of Remote Vegetated Areas. Water 2020, Vol. 12, Page 2745, 12(10), 2745. https://doi.org/10.3390/W12102745

Rennó, C. D., Nobre, A. D., Cuartas, L. A., Soares, J. V., Hodnett, M. G., Tomasella, J., & Waterloo, M. J. (2008). HAND, a new terrain descriptor using SRTM-DEM: Mapping terra-firme rainforest environments in Amazonia. Remote Sensing of Environment, 112(9), 3469–3481. https://doi.org/10.1016/j.rse.2008.03.018

Romali, N. S., & Yusop, Z. (2021). Flood damage and risk assessment for urban area in Malaysia. Hydrology Research, 52(1), 142–159. https://doi.org/10.2166/NH.2020.121

Sadeh, Y., Zhu, X., Dunkerley, D., Walker, J. P., Zhang, Y., Rozenstein, O., Manivasagam, V. S., & Chenu, K. (2021). Fusion of Sentinel-2 and PlanetScope time-series data into daily 3 m surface reflectance and wheat LAI monitoring. International Journal of Applied Earth Observation and Geoinformation, 96, 102260. https://doi.org/10.1016/J.JAG.2020.102260

Sai, V., Vanama, K., Mandal, D., & Rao, Y. S. (2020). GEE4FLOOD: rapid mapping of flood areas using temporal Sentinel-1 SAR images with Google Earth Engine cloud platform. Journal of Applied Remote Sensing, 14(3). https://doi.org/10.1117/1.JRS.14.034505

Sit, M. A., Seo, B., & Demir, I. (2023). TempNet–temporal super-resolution of radar rainfall products with residual CNNs. Journal of hydroinformatics, 25(2), 552-566.

Teng, J., Jakeman, A. J., Vaze, J., Croke, B. F. W., Dutta, D., & Kim, S. (2017). Flood inundation modelling: A review of methods, recent advances and uncertainty analysis. In

Environmental Modelling and Software (Vol. 90, pp. 201–216). https://doi.org/10.1016/j.envsoft.2017.01.006

Thakur, P. K., Ranjan, R., Singh, S., Dhote, P. R., Sharma, V., Srivastav, V., Dhasmana, M., Aggarwal, S. P., Chauhan, P., Nikam, B. R., Garg, V., & Chouksey, A. (2020). SYNERGISTIC USE OF REMOTE SENSING, GIS AND HYDROLOGICAL MODELS FOR STUDY OF AUGUST 2018 KERALA FLOODS. The International Archives of the Photogrammetry, Remote Sensing and Spatial Information Sciences, Volume XLIII-B3-2020. https://doi.org/10.5194/isprs-archives-XLIII-B3-2020-1263-2020

Thapa, A., Horanont, T., & Neupane, B. (2022). Parcel-Level Flood and Drought Detection for Insurance Using Sentinel-2A, Sentinel-1 SAR GRD and Mobile Images. Remote Sensing 2022, Vol. 14, Page 6095, 14(23), 6095. https://doi.org/10.3390/RS14236095

Tiwari, V., Kumar, V., Matin, M. A., Thapa, A., Ellenburg, W. L., Gupta, N., & Thapa, S. (2020). Flood inundation mapping-Kerala 2018; Harnessing the power of SAR, automatic threshold detection method and Google Earth Engine. PLoS ONE, 15(8 August), e0237324. https://doi.org/10.1371/journal.pone.0237324

Tsyganskaya, V., Martinis, S., Marzahn, P., & Ludwig, R. (2018). Detection of temporary flooded vegetation using Sentinel-1 time series data. Remote Sensing, 10(8), 1286. https://doi.org/10.3390/rs10081286

Tsyganskaya, V., Martinis, S., Twele, A., Cao, W., Schmitt, A., Marzahn, P., & Ludwig, R. (2016). A fuzzy logic-based approach for the detection of flooded vegetation by means of synthetic aperture radar data. International Archives of the Photogrammetry, Remote Sensing and Spatial Information Sciences - ISPRS Archives, 41, 371–378. https://doi.org/10.5194/isprsarchives-XLI-B7-371-2016

Tulbure, M. G., Broich, M., Perin, V., Gaines, M., Ju, J., Stehman, S. V., Pavelsky, T., Masek, J. G., Yin, S., Mai, J., & Betbeder-Matibet, L. (2022). Can we detect more ephemeral floods with higher density harmonized Landsat Sentinel 2 data compared to Landsat 8 alone? ISPRS Journal of Photogrammetry and Remote Sensing, 185, 232–246. https://doi.org/10.1016/J.ISPRSJPRS.2022.01.021

Twele, A., Cao, W., Plank, S., & Martinis, S. (2016). Sentinel-1-based flood mapping: a fully automated processing chain. International Journal of Remote Sensing, 37(13), 2990–3004. https://doi.org/10.1080/01431161.2016.1192304

Uddin, K., Matin, M. A., & Meyer, F. J. (2019). Operational Flood Mapping Using Multi-Temporal Sentinel-1 SAR Images: A Case Study from Bangladesh. Remote Sensing 2019, Vol. 11, Page 1581, 11(13), 1581. https://doi.org/10.3390/RS11131581

U.S. Army Corps of Engineers. (2016). Upper Mississippi River Restoration (UMRR) Program Long Term Resource Monitoring (LTRM) element. https://doi.org/10.5066/F7057CZ3

US Department of Commerce, N. N. W. S. (n.d.). Summary of Major Flooding along Mississippi River in 2019.

Wu, W., Shao, Z., Huang, X., Teng, J., Guo, S., & Li, D. (2022). Quantifying the sensitivity of SAR and optical images three-level fusions in land cover classification to registration errors.

International Journal of Applied Earth Observation and Geoinformation, 112, 102868. https://doi.org/10.1016/J.JAG.2022.102868

Yan, K., Di Baldassarre, G., Solomatine, D. P., & Schumann, G. J. P. (2015). A review of low-cost space-borne data for flood modelling: topography, flood extent and water level. Hydrological Processes, 29(15), 3368–3387. https://doi.org/10.1002/HYP.10449

Yildirim, E., & Demir, I. (2022). Agricultural flood vulnerability assessment and risk quantification in Iowa. Science of The Total Environment, 826, 154165.

Zhai, H., Zhang, H., Zhang, L., & Li, P. (2018). Cloud/shadow detection based on spectral indices for multi/hyperspectral optical remote sensing imagery. ISPRS Journal of Photogrammetry and Remote Sensing, 144, 235–253. https://doi.org/10.1016/J.ISPRSJPRS.2018.07.006